

# Effect of Calcium on the Formation and Protectiveness of Iron Carbonate Layer in CO<sub>2</sub> Corrosion

Saba Navabzadeh Esmaeely,<sup>‡,\*</sup> Yoon-Seok Choi,<sup>\*</sup> David Young,<sup>\*</sup> and Srdjan Nešić<sup>\*</sup>

## ABSTRACT

The effect of calcium (Ca<sup>2+</sup>) on the carbon dioxide (CO<sub>2</sub>) corrosion of mild steel was investigated in simulated saline aquifer environments (1 wt% sodium chloride [NaCl], 80°C, pH 6.6) with different concentrations of Ca<sup>2+</sup> (10, 100, 1,000, and 10,000 ppm). Electrochemical methods (open-circuit potential [OCP]) and linear polarization resistance [LPR] measurements were used to evaluate the corrosion behavior. Surface analysis techniques (scanning electron microscopy [SEM], energy-dispersive x-ray spectroscopy [EDS], and x-ray diffraction [XRD]) were used to characterize the morphology and identity the corrosion products. The results showed that with low concentrations of Ca<sup>2+</sup> (10 ppm and 100 ppm), the corrosion rate decreased with time as a result of the formation of protective iron carbonate (FeCO<sub>3</sub>) and/or mixed carbonate (Fe<sub>x</sub>Ca<sub>y</sub>CO<sub>3</sub>) (x + y = 1). However, the presence of high concentrations of Ca<sup>2+</sup> (1,000 ppm and 10,000 ppm) resulted in the change of corrosion product from protective FeCO<sub>3</sub> to non-protective calcium carbonate (CaCO<sub>3</sub>), and an increasing corrosion rate with time. Results of surface analysis revealed a different steel surface morphology with pitting observed in the presence of 10,000 ppm Ca<sup>2+</sup>.

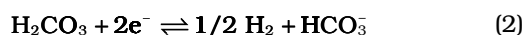
**KEY WORDS:** Ca<sup>2+</sup>, CaCO<sub>3</sub>, carbon capture and storage, Fe<sup>2+</sup>, FeCO<sub>3</sub>, localized corrosion

## INTRODUCTION

The carbon capture and storage (CCS) process contains three stages:

- carbon dioxide (CO<sub>2</sub>) capture at its generation source (coal or gas-fired power plant, refinery, syngas unit, cement works, or some other industrial process)
- transportation to the geologic storage site (usually by pipeline transmission)
- injection into geologic host reservoirs<sup>1</sup>

Among the known options in CCS, injection and storage of CO<sub>2</sub> in deep saline aquifers has the potential to cause casing corrosion because of the direct contact between injected CO<sub>2</sub> and the saline aquifer with highly concentrated aqueous salts such as sodium chloride (NaCl) and calcium chloride (CaCl<sub>2</sub>). Aqueous CO<sub>2</sub> is known as a corrosive agent. Studies have been performed on CO<sub>2</sub> corrosion at high pressures. All studies showed that the initial “bare steel” corrosion rate at high partial pressure CO<sub>2</sub> (~70 bars) is very high.<sup>2-3</sup> For high pressure CO<sub>2</sub> the concentration of hydrogen ions ([H<sup>+</sup>]) is rather high, as a result of the excessive amount of carbonic acid (H<sub>2</sub>CO<sub>3</sub>) and, hence, its dissociation. Also, the presence of H<sub>2</sub>CO<sub>3</sub> can provide another pathway for the cathodic reaction:<sup>2</sup>



In stagnant conditions, the system may reach favorable conditions for formation of FeCO<sub>3</sub>, when the cor-

Submitted for publication: February 5, 2013. Revised and accepted: May 2, 2013. Preprint available online: May 31, 2013. doi: <http://dx.doi.org/10.5006/0942>.

<sup>‡</sup> Corresponding author. E-mail: [navabzadeh.saba@gmail.com](mailto:navabzadeh.saba@gmail.com).

<sup>\*</sup> Institute for Corrosion and Multiphase Technology, Department of Chemical and Biomolecular Engineering, Ohio University, Ohio, 45701.

rosion rate starts to decrease.<sup>3</sup> Even though the bulk pH remains very low (~pH 3) at a very high pressure of CO<sub>2</sub>, there is a high concentration of Fe<sup>2+</sup> near the surface because of the high corrosion rate. This would create favorable conditions for iron carbonate (FeCO<sub>3</sub>) precipitation.

The role of FeCO<sub>3</sub> formation during the corrosion process has been studied over the past few decades.<sup>4-8</sup> Nešić suggested that FeCO<sub>3</sub> is protective when it is dense and adhesive at the steel surface, because such a layer retards the transportation of corrosive species toward the steel surface and blocks portions of the steel surface making them unavailable for corrosion.<sup>9</sup> The corrosion product layer properties in terms of both structure and composition have been studied in recent years.<sup>10-13</sup> Different parameters affect the formation of FeCO<sub>3</sub> and its diffusion-limiting properties.<sup>9,14</sup> The chemical and mechanical properties of the layer formed on the surface are a function of many factors, such as temperature, supersaturation, and chemical composition of the layer.<sup>14-16</sup> Ingham, et al., reported an enhancement in protectiveness of the corrosion product layer when a small concentration of magnesium (Mg<sup>2+</sup>) was present.<sup>17</sup>

Calcium carbonate (CaCO<sub>3</sub>) is isostructural with FeCO<sub>3</sub>. Therefore, Ca<sup>2+</sup> readily incorporates into the FeCO<sub>3</sub> structure and vice versa.<sup>18</sup> Therefore, the properties of FeCO<sub>3</sub>, both morphologically and chemically, in the presence of Ca<sup>2+</sup>, are subject to change. It has been established already that the morphology of FeCO<sub>3</sub> plays a significant role in the corrosion process.<sup>19-20</sup> While many studies have addressed the different parametric effects on the formation and protectiveness of FeCO<sub>3</sub>,<sup>8-9,14,16,19-21</sup> the role of brine chemistry, particularly in terms of the effect of individual ions on corrosion product layer formation, was not studied in great detail.<sup>17</sup> For example, one of the important species in brines is Ca<sup>2+</sup>, which can be present at high concentrations (up to 30,000 ppm).<sup>22</sup> However, effects of Ca<sup>2+</sup> on corrosion mechanisms have not been well documented.

Little has been reported on the effect of Ca<sup>2+</sup> on corrosion in the literature, with findings often appearing contradictory. Zhao, et al.,<sup>23-24</sup> claimed that corrosion rate decreased in the “short term” in the presence of Ca<sup>2+</sup> and Mg<sup>2+</sup>, but there was no special difference in “long-term exposure.” Ding, et al., reported the corrosion rate increased with an increase in the Ca<sup>2+</sup> concentration.<sup>25</sup> Jiang, et al., reported pitting associated with CaCl<sub>2</sub>. They claimed that while Cl<sup>-</sup> caused pitting, the presence of Ca<sup>2+</sup> postponed the initiation of the pitting.<sup>26</sup> Ren, et al.,<sup>27</sup> as well as Zhu, et al.,<sup>28</sup> reported pitting with reference to the presence of Cl<sup>-</sup>

**TABLE 1**  
*Test Matrix*

Parameters	Conditions
Total Pressure	0.1 MPa
pCO <sub>2</sub>	0.05 MPa
Temperature	80°C
Solution	1 wt% NaCl
pH	6.6
Flow condition	Stagnant
Steel	G10180

**TABLE 2**  
*Test Conditions*

Test Condition No.	Initial Concentrations of Fe <sup>2+</sup> and Ca <sup>2+</sup>
1	10 ppm Fe <sup>2+</sup>
2	10 ppm Fe <sup>2+</sup> + 10 ppm Ca <sup>2+</sup>
3	10 ppm Fe <sup>2+</sup> + 100 ppm Ca <sup>2+</sup>
4	10 ppm Fe <sup>2+</sup> + 1,000 ppm Ca <sup>2+</sup>
5	10 ppm Fe <sup>2+</sup> + 10,000 ppm Ca <sup>2+</sup>

in CaCl<sub>2</sub>-containing electrolytes. Gao, et al.,<sup>29</sup> reported pitting in conjunction with the formation of Fe<sub>x</sub>Ca<sub>y</sub>CO<sub>3</sub> and Fe<sub>x</sub>(Mg,Ca)<sub>y</sub>CO<sub>3</sub> (x + y = 1) on the steel surface. A broader review of the literature indicates that Cl<sup>-</sup> ions are often associated with pitting; however, the role of overall water chemistry, and in particular Ca<sup>2+</sup> ions, is generally not clear. In many instances, some of the key parameters are not measured or reported; for example, the pH of the aqueous solution is often “unknown” making any discussion of the results unconvincing. In CO<sub>2</sub> corrosion of mild steel, only higher pH is associated with the formation of protective FeCO<sub>3</sub> layers; therefore, any influence of Ca<sup>2+</sup> concentration must be analyzed in the context of the overall water chemistry effects.

Although CO<sub>2</sub> is stored in liquid or supercritical phase at high pressure, the effect of Ca<sup>2+</sup> on FeCO<sub>3</sub> formation is not known even if at low CO<sub>2</sub> partial pressures. Therefore, the work reported, conducted at low CO<sub>2</sub> partial pressures, can be considered as a preliminary study on the effect of Ca<sup>2+</sup> in saline aquifers on corrosion of casing steel related to the injection of CO<sub>2</sub> for its geologic storage.

## EXPERIMENTAL PROCEDURES

Experiments were conducted in a 2-L glass cell using a three-electrode setup. In each experiment, three flat specimens made from AISI<sup>(1)</sup> 1018 mild steel (UNS G10180)<sup>(2)</sup> with an exposed area of 5.4 cm<sup>2</sup> were used for electrochemical measurement and for surface analysis. Prior to insertion, the specimens were wet-polished with silicon carbide (SiC) paper, down to 600 grit, and rinsed with isopropyl alcohol (C<sub>3</sub>H<sub>8</sub>O) in an ultrasonic bath and dried.

Tables 1 and 2 show the test matrix and test conditions, respectively. The glass cell was filled with

<sup>(1)</sup> American Iron and Steel Institute, 25 Massachusetts Ave., NW Ste. 800, Washington, DC 20001.

<sup>(2)</sup> UNS numbers are listed in *Metals and Alloys in the Unified Numbering System*, published by the Society of Automotive Engineers (SAE International) and cosponsored by ASTM International.

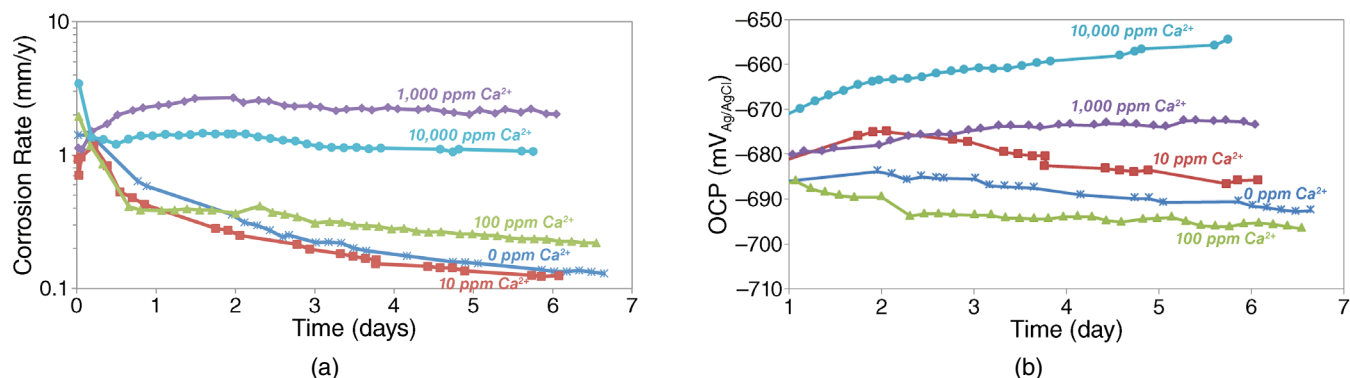


**FIGURE 1.** Variations of (a) corrosion rate and (b) OCP for mild steel exposed to a simulated brine with different initial concentrations of Ca<sup>2+</sup> at 80°C and pCO<sub>2</sub> of 0.05 MPa with 10 ppm Fe<sup>2+</sup>.

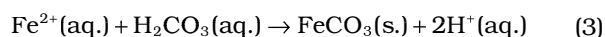
2 L of 1 wt% NaCl electrolyte (prepared with deionized water). The solution was stirred with a magnetic stirrer and the temperature was set to 80°C; CO<sub>2</sub> gas was purged continuously through the solution. The solution pH was adjusted to 6.6 by addition of a deoxygenated 1.0 M sodium hydroxide (NaOH) solution. After the pH stabilized, the magnetic stir bar was stopped and samples were inserted into the glass cell.

The corrosion behavior was monitored by electrochemical methods: open-circuit potential (OCP) and linear polarization resistance (LPR) measurements. Samples from all experiments were characterized by x-ray diffraction (XRD), scanning electron microscopy (SEM), energy-dispersive x-ray spectroscopy (EDS), and infinite focus microscopy (IFM) to investigate the effect of Ca<sup>2+</sup> on the morphology and composition of the corrosion product layer. The Ca<sup>2+</sup> concentration was measured using inductively coupled plasma (ICP) spectroscopy. Analyses for the Fe<sup>2+</sup> concentration were performed with a spectrophotometer.

At the end of each experiment and after completion of the corrosion product surface analysis, one sample from each experiment was treated with Clarke solution, according to ASTM G1, to remove the corrosion product layer and scan the underlying metal surface.<sup>30</sup>

## RESULTS

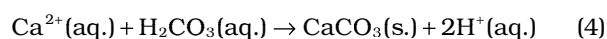
Figure 1 shows the variations of OCP and corrosion rate with time for each experiment condition. As shown in Figure 1(a), the corrosion rate decreased with time for the low initial Ca<sup>2+</sup> concentration conditions. This indicates that a protective FeCO<sub>3</sub> layer was formed on the steel surface according to:



When a FeCO<sub>3</sub> layer forms on the mild steel surface, it can slow down corrosion by presenting a diffusion barrier for the species involved in the process, and by blocking (covering) a portion of the steel sur-

face and preventing the underlying steel from undergoing further oxidative dissolution.<sup>9,31</sup>

For the low initial Ca<sup>2+</sup> concentration conditions (0, 10, and 100 ppm), the formation of a protective FeCO<sub>3</sub> layer apparently occurred without significant interference by Ca<sup>2+</sup> ions. However, the corrosion behavior of mild steel with higher initial Ca<sup>2+</sup> concentrations of 1,000 ppm and 10,000 ppm was different. Pots and Kapusta reported that a mixed iron and calcium carbonate layer is not protective and “stable.”<sup>32</sup> In the experiments with high Ca<sup>2+</sup> concentrations, the corrosion rate did not decrease with time, which is likely from the lack of formation of a protective FeCO<sub>3</sub> layer on the steel surface. At this stage it can be hypothesized that this was caused by a lower pH, seen in experiments with higher initial Ca<sup>2+</sup> concentrations, as shown in Figure 2(a). Note that precipitation of CaCO<sub>3</sub> in aqueous CO<sub>2</sub> solutions will lead to acidification, as the equilibrium pH is approached:



To illustrate this, Figure 2(b) shows the variation of FeCO<sub>3</sub> saturation degree with time. The saturation degree (S) was calculated by Equation (3), based on the measured values of pH and Fe<sup>2+</sup> concentration. The CO<sub>3</sub><sup>2-</sup> concentration was calculated using a simple equilibrium model for aqueous CO<sub>2</sub> species.<sup>33</sup>

$$S_{\text{FeCO}_3} = \frac{C(\text{Fe}^{2+}) * C(\text{CO}_3^{2-})}{K_{\text{SP,FeCO}_3}} \quad (5)$$

The  $K_{\text{sp,FeCO}_3}$  is the solubility product of FeCO<sub>3</sub> calculated as:<sup>34</sup>

$$\text{Log}K_{\text{SP,FeCO}_3} = -59.3498 - 0.041377 * T - \frac{2.11963}{T} + 24.5724\text{Log}(T) + 2.518 * I^{0.5} - 0.6578 * I \quad (6)$$

T is temperature in Kelvin and I is ionic strength.

As shown in Figure 2(b), the experiments with lower Ca<sup>2+</sup> concentrations remained highly supersatu-

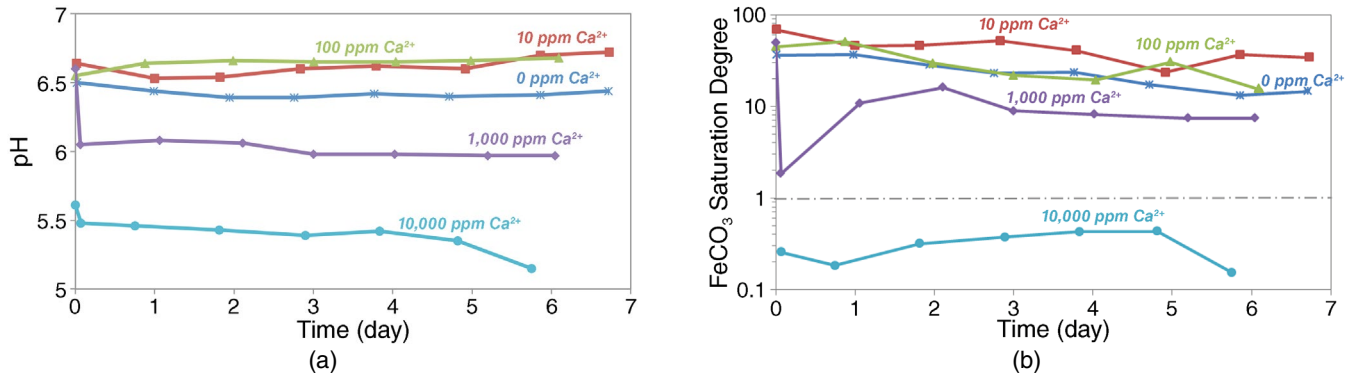


**FIGURE 2.** Variations of (a) pH and (b) saturation degree of FeCO<sub>3</sub> for mild steel exposed to a simulated brine with different/varying concentrations of Ca<sup>2+</sup> at 80°C and pCO<sub>2</sub> of 0.05 MPa with 10 ppm Fe<sup>2+</sup>.

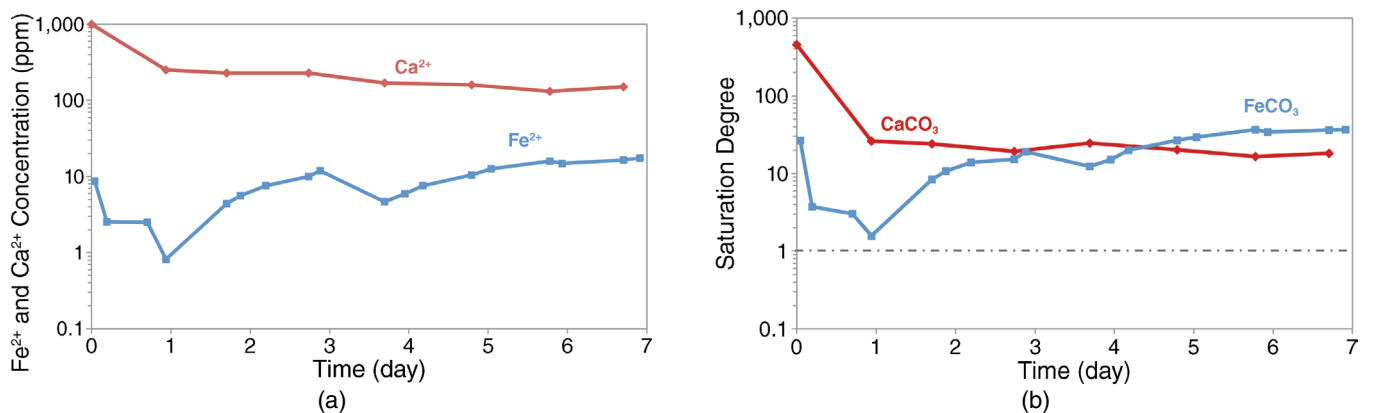


**FIGURE 3.** (a) Fe<sup>2+</sup> and Ca<sup>2+</sup> concentrations and (b) CaCO<sub>3</sub> and FeCO<sub>3</sub> saturation degree for the initial 1,000 ppm Ca<sup>2+</sup> system vs. time at 80°C and pCO<sub>2</sub> of 0.05 MPa with 10 ppm Fe<sup>2+</sup>.

rated with respect to FeCO<sub>3</sub> during the whole experiment, leading to steady precipitation of protective FeCO<sub>3</sub>. The experiment with initial Ca<sup>2+</sup> concentration of 1,000 ppm was also supersaturated with respect to FeCO<sub>3</sub>, while at the initial Ca<sup>2+</sup> concentration of 10,000 ppm, the rapid precipitation of CaCO<sub>3</sub> made the solution under-saturated with respect to FeCO<sub>3</sub>, making it impossible for the protective FeCO<sub>3</sub> layer to form.

To explain this behavior in more detail, let us now focus on the experiment with initial Ca<sup>2+</sup> concentration of 1,000 ppm. The measured variations of Fe<sup>2+</sup> concentration and Ca<sup>2+</sup> concentration with time are plotted in Figure 3(a). The concentration of Ca<sup>2+</sup> decreased steadily as a result of the precipitation of CaCO<sub>3</sub>. The Fe<sup>2+</sup> concentration initially decreased because of the precipitation of FeCO<sub>3</sub> from a supersaturated solution, and then as the saturation level was approached, the Fe<sup>2+</sup> concentration increased from the high general corrosion rate (Figure 1[a]).

The corresponding saturation degrees with respect to CaCO<sub>3</sub> and FeCO<sub>3</sub> vs. time are given in Figure 3(b). There, based on the measured pH and Ca<sup>2+</sup>, the saturation degree with respect to CaCO<sub>3</sub> was calculated according to:

$$S_{\text{CaCO}_3} = \frac{C(\text{Ca}^{2+}) * C(\text{CO}_3^{2-})}{K_{\text{SP,CaCO}_3}} \quad (7)$$

where  $K_{\text{sp,CaCO}_3}$  is the solubility product of CaCO<sub>3</sub> calculated as:<sup>35</sup>

$$\text{Log}K_{\text{sp,CaCO}_3} = -1228.732 - 0.299444 * T + \frac{35512.75}{T} + 485.818 \text{Log}T \quad (8)$$

T is temperature in Kelvin and I is ionic strength.

As is shown in Figure 3, because of a very high initial concentration of Ca<sup>2+</sup>, the aqueous solution was initially highly supersaturated with respect to CaCO<sub>3</sub>. This led to the precipitation of CaCO<sub>3</sub> reducing the level of saturation. As the CaCO<sub>3</sub> supersaturation level approached 10, the driving force for CaCO<sub>3</sub> precipitation decreased and the concentration of calcium changed very slowly. At the same time the Fe<sup>2+</sup> concentration initially decreased much more rapidly than the Ca<sup>2+</sup> concentration, even if the initial level of supersaturation with respect to FeCO<sub>3</sub> was much lower than that of CaCO<sub>3</sub>, pointing to a much faster kinetics. As the level of FeCO<sub>3</sub> supersaturation fell below 10, the kinetics of FeCO<sub>3</sub> precipitation decreased,

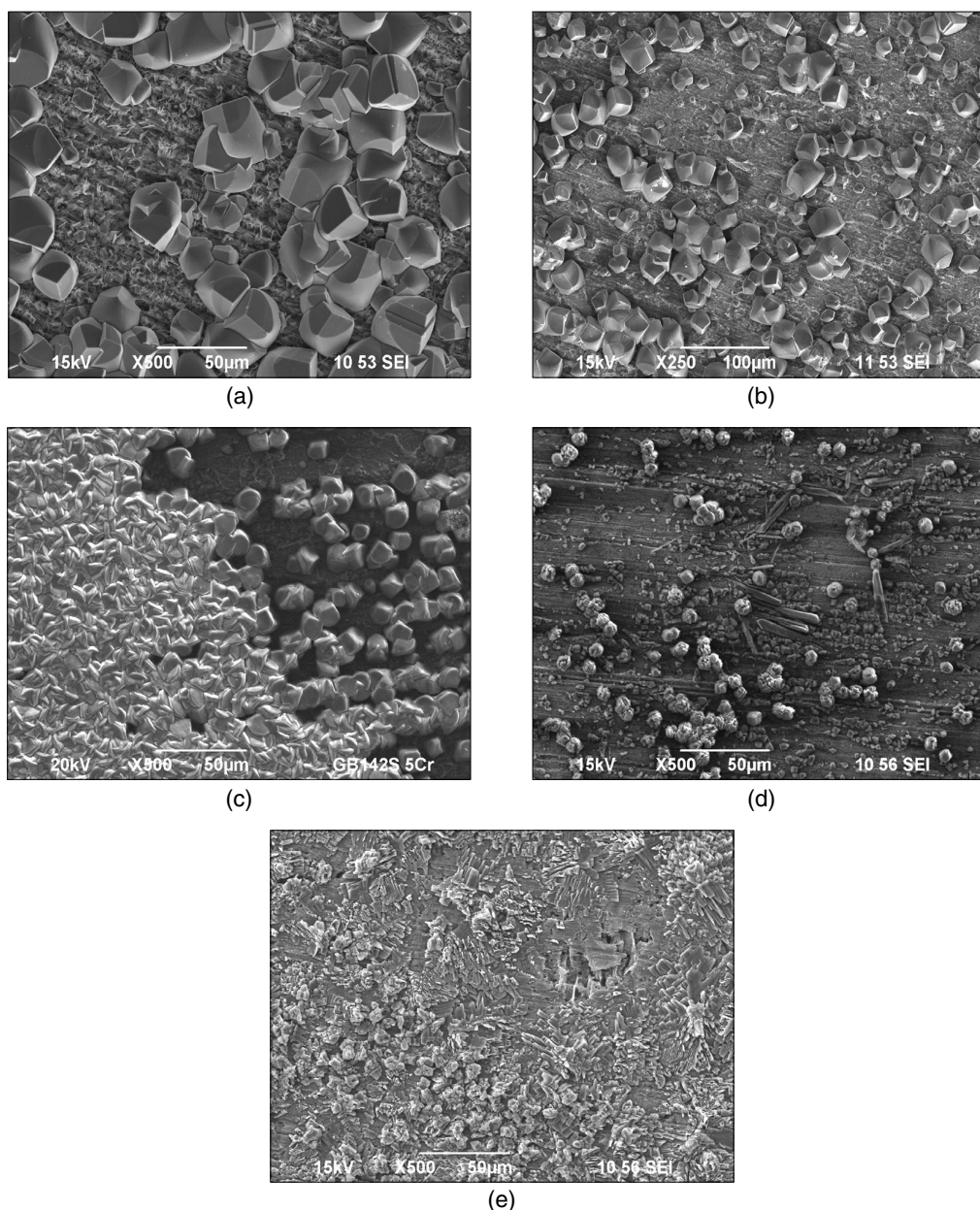


**FIGURE 4.** SEM images of recovered samples (UNS G10180) from experiments conducted at 80°C and  $p\text{CO}_2$  of 0.05 MPa with 10 ppm  $\text{Fe}^{2+}$  for (a) 0 ppm  $\text{Ca}^{2+}$ , (b) 10 ppm  $\text{Ca}^{2+}$ , (c) 100 ppm  $\text{Ca}^{2+}$ , (d) 1,000 ppm  $\text{Ca}^{2+}$ , and (e) 10,000 ppm  $\text{Ca}^{2+}$ .

while at the same time the corrosion rate remained unchanged (Figure 1[a]), which led to an increase in  $\text{Fe}^{2+}$  concentration over time.

Figure 4 shows the SEM images of specimens from electrolytes with 0 ppm  $\text{Ca}^{2+}$ , 10 ppm  $\text{Ca}^{2+}$ , 100 ppm  $\text{Ca}^{2+}$ , 1,000 ppm  $\text{Ca}^{2+}$ , and 10,000 ppm  $\text{Ca}^{2+}$ . Analyses for the experiments with 0, 10, and 100 ppm  $\text{Ca}^{2+}$  show scattered crystals of  $\text{FeCO}_3$  on the surface; corrosion product crystal morphologies did not appreciably change at these relatively low  $\text{Ca}^{2+}$  concentrations. However, at higher  $\text{Ca}^{2+}$  concentrations, as shown in Figures 4(d) and (e) for 1,000 ppm  $\text{Ca}^{2+}$  and 10,000 ppm  $\text{Ca}^{2+}$ , respectively, the crystal morphologies at the surface significantly changed as a result of the presence

of  $\text{Ca}^{2+}$ . In the experiment with 1,000 ppm  $\text{Ca}^{2+}$ , the crystals were mostly elongated. For the electrolyte with 10,000 ppm  $\text{Ca}^{2+}$ , the surface was covered with a dense, intergrown layer of scale rather than being comprised of relatively discrete crystals.

Figure 5 represents the XRD data of specimens tested with 0 ppm  $\text{Ca}^{2+}$ , 10 ppm  $\text{Ca}^{2+}$ , 100 ppm  $\text{Ca}^{2+}$ , 1,000 ppm  $\text{Ca}^{2+}$ , and 10,000 ppm  $\text{Ca}^{2+}$ . The XRD data in Figure 5(a) confirm the presence of  $\text{FeCO}_3$  on the surface. Shown in Figure 5(b), based on the XRD data, it can be concluded that a thick and protective layer was formed on the surface, because the main peak of  $\alpha\text{-Fe}$  related to diffraction from the steel substrate cannot be detected. The XRD data shows less intense,

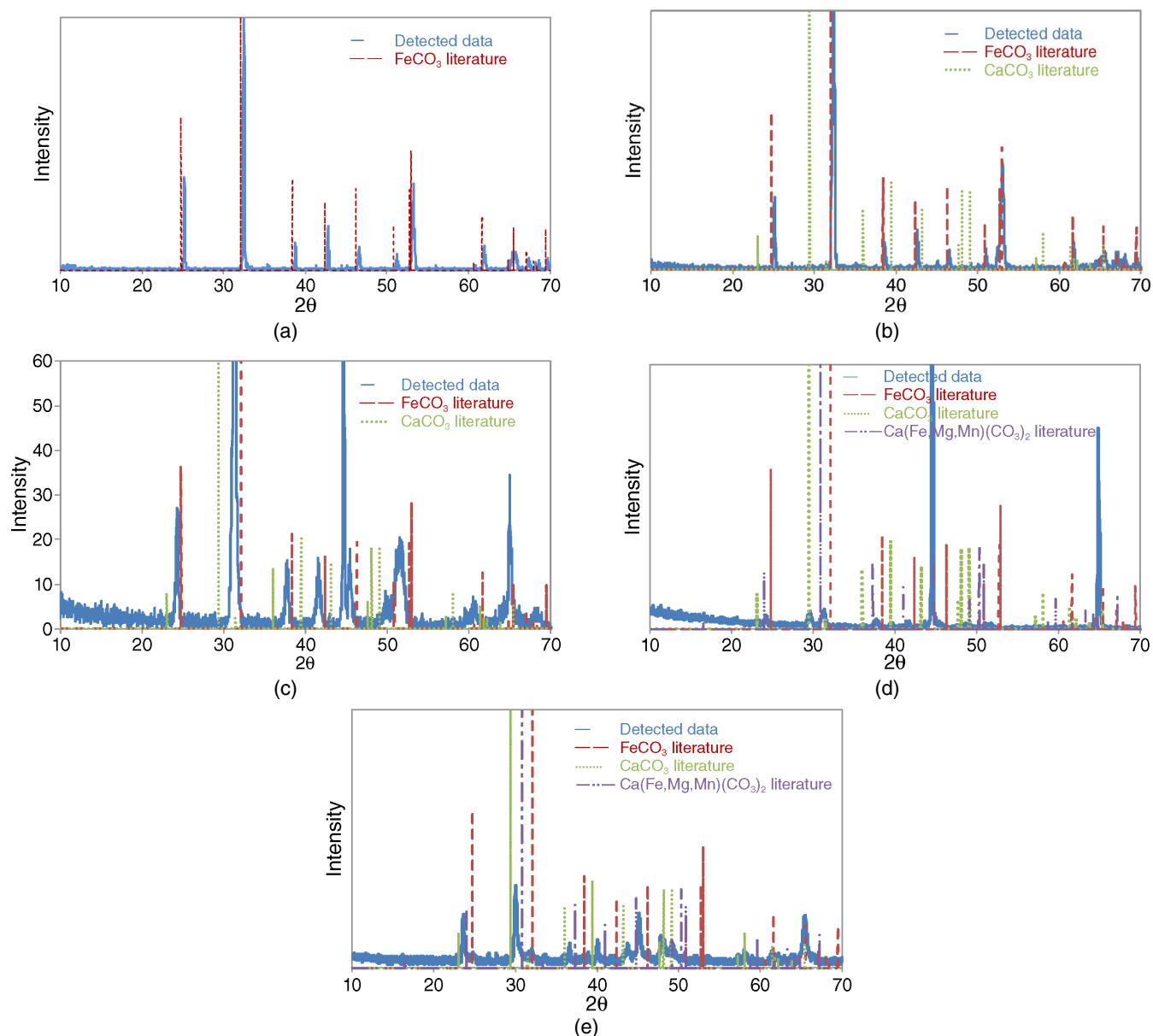


**FIGURE 5.** XRD data of recovered samples (UNS G10180) from experiments conducted at 80°C and  $p\text{CO}_2$  0.05 MPa with 10 ppm  $\text{Fe}^{2+}$  for (a) 0 ppm  $\text{Ca}^{2+}$ , (b) 10 ppm  $\text{Ca}^{2+}$ , (c) 100 ppm  $\text{Ca}^{2+}$ , (d) 1,000 ppm  $\text{Ca}^{2+}$ , and (e) 10,000 ppm  $\text{Ca}^{2+}$ .

broadened, and shifted peaks as a result of the substitution of the larger  $\text{Ca}^{2+}$  for  $\text{Fe}^{2+}$  in the  $\text{FeCO}_3$  structure. This results in the formation of a solid solution with the formula  $\text{Fe}_x\text{Ca}_y\text{CO}_3$  ( $x + y = 1$ ). According to Figure 5(c), similar to the experiment condition no. 2 with the addition of 10 ppm  $\text{Ca}^{2+}$ , the XRD data again shows broadened and shifted peaks relative to  $\text{FeCO}_3$  with their more profound differences, compared with Figure 5(b), being from the higher concentration of  $\text{Ca}^{2+}$  in the electrolyte. Consequently, this is a consequence of greater substitution of  $\text{Fe}^{2+}$  with  $\text{Ca}^{2+}$  during formation of the solid solution; compositional complexity and concentration gradients within the  $\text{Fe}_x\text{Ca}_y\text{CO}_3$  scale is reflected by significant asymmetry in the principle diffraction peaks between 30 and 32  $2\theta$ .

The XRD data shown in Figure 5(d) is indicative of a transition to a physical mixture of  $\text{CaCO}_3$  with a solid solution of  $\text{Fe}_x\text{Ca}_y\text{CO}_3$  on the steel surface. The high corrosion rate in this experiment may be the result of the formation of mostly  $\text{CaCO}_3$  rather than  $\text{FeCO}_3$  or  $\text{Fe}_x\text{Ca}_y\text{CO}_3$  on the surface. This would indicate that  $\text{CaCO}_3$  is not as protective as  $\text{FeCO}_3$  or  $\text{Fe}_x\text{Ca}_y\text{CO}_3$ . According to the XRD data shown in Figure 5(e), there is a physical mixture of the  $\text{CaCO}_3$  and a solid solution of  $\text{Fe}_x\text{Ca}_y\text{CO}_3$  on the surface. The high corrosion rate in this experiment is likely the result of the formation of mostly  $\text{Fe}_x\text{Ca}_y\text{CO}_3$  with a high concentration of  $\text{Ca}^{2+}$  on the steel surface.

Figure 6 shows the cross-sectional analysis of the tested conditions with 0, 10, 1,000, and 10,000 ppm

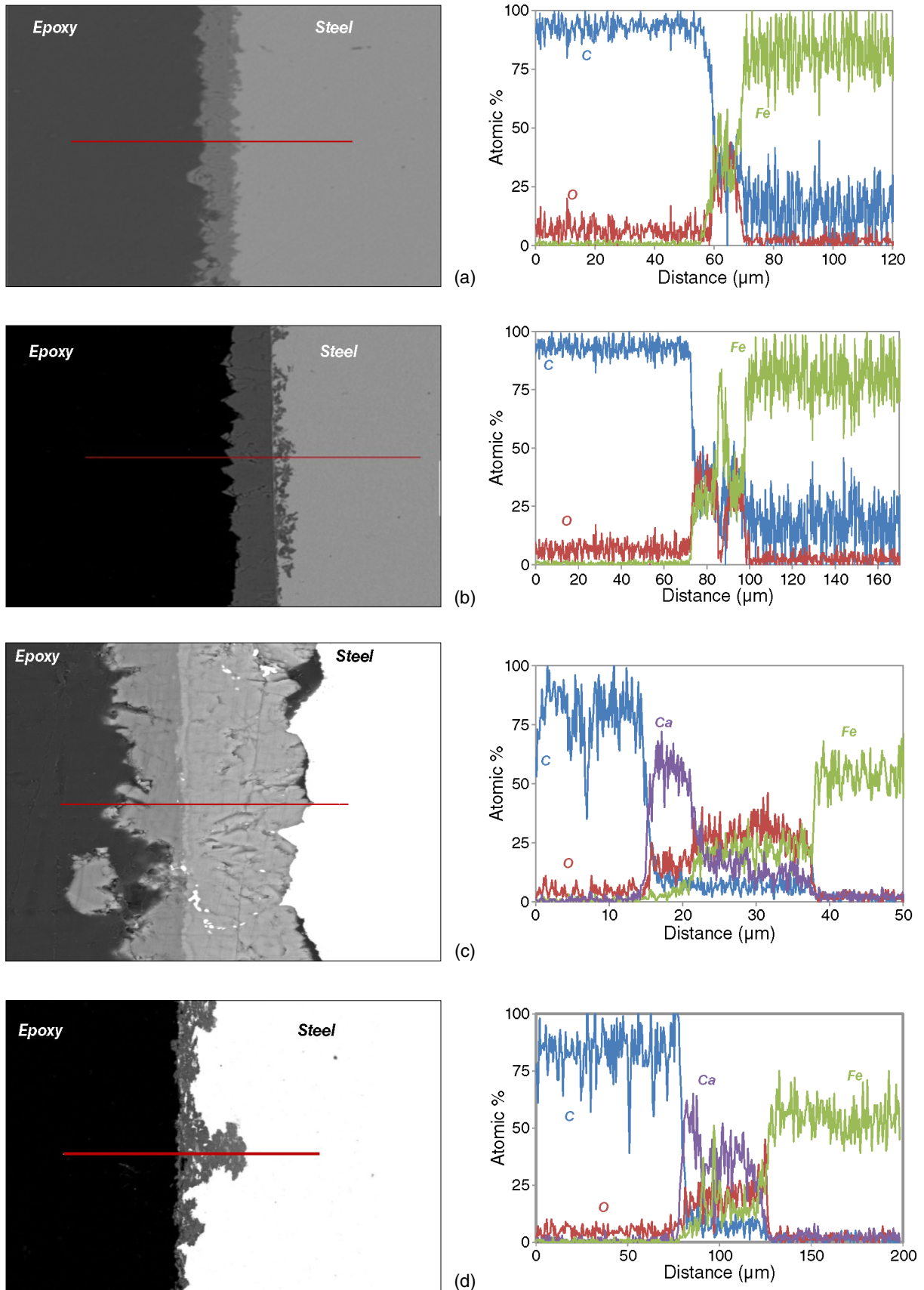


**FIGURE 6.** Cross-sectional image and EDS spectra of samples (G10180) recovered from experiments at 80°C and  $p\text{CO}_2$  0.05 MPa with 10 ppm  $\text{Fe}^{2+}$  and (a) 0 ppm  $\text{Ca}^{2+}$ , (b) 10 ppm  $\text{Ca}^{2+}$ , (c) 1,000 ppm  $\text{Ca}^{2+}$ , and (d) 10,000 ppm  $\text{Ca}^{2+}$ .

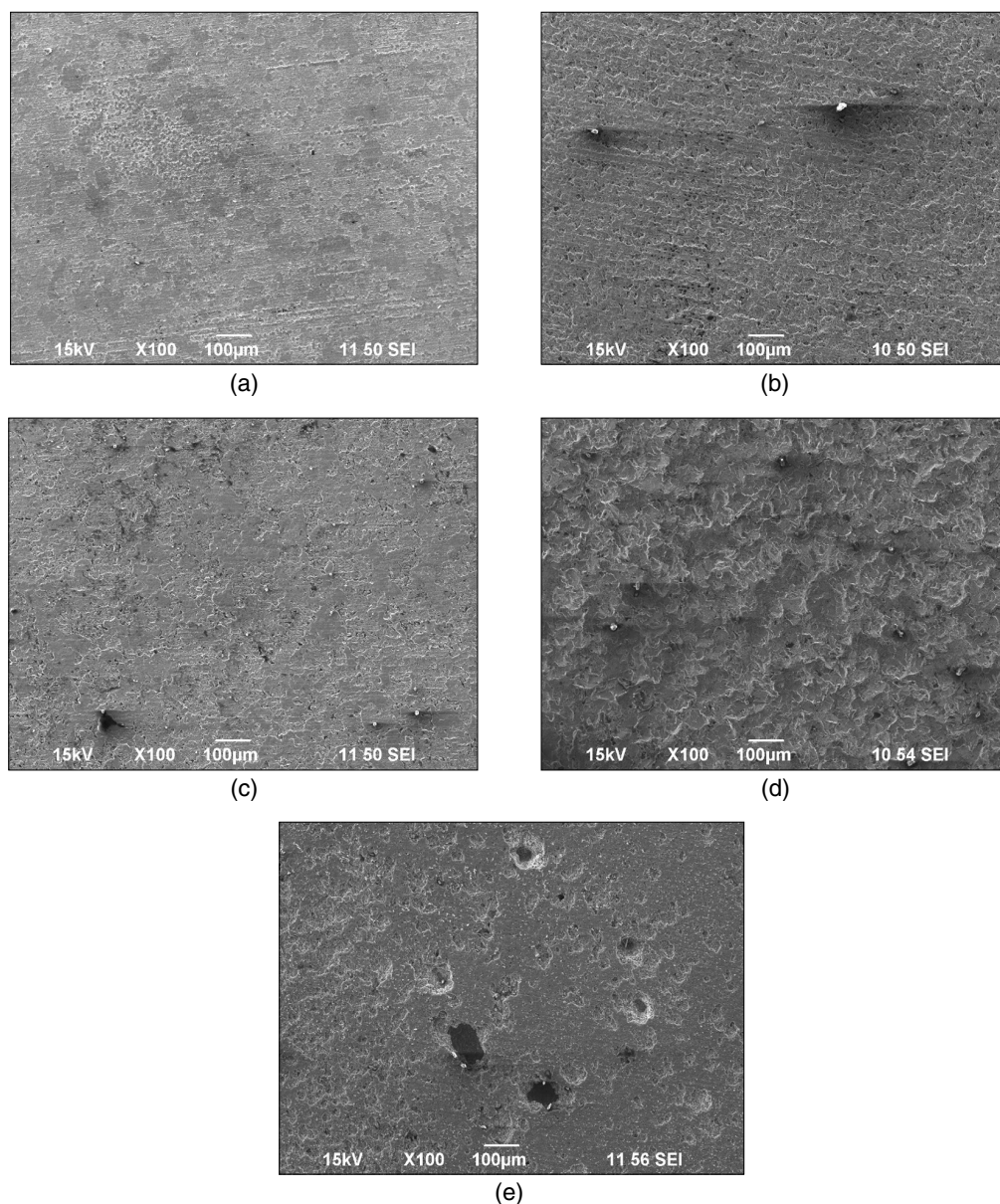


**FIGURE 7.** Surfaces after corrosion product removal from samples (UNS G10180) for experiments conducted at 80°C and  $p\text{CO}_2$  0.05 MPa with 10 ppm  $\text{Fe}^{2+}$  and (a) 0 ppm  $\text{Ca}^{2+}$ , (b) 10 ppm  $\text{Ca}^{2+}$ , (c) 100 ppm  $\text{Ca}^{2+}$ , (d) 1,000 ppm  $\text{Ca}^{2+}$ , and (e) 10,000 ppm  $\text{Ca}^{2+}$ .

$\text{Ca}^{2+}$  (note that the cross section from the 100 ppm  $\text{Ca}^{2+}$  experiment was not available). As is shown in Figures 6(a) and (b), there is not a significant difference in the layer on the surface between 0 and 10 ppm  $\text{Ca}^{2+}$ . On the other hand, in the presence of 1,000 ppm  $\text{Ca}^{2+}$ , two different layers on the steel surface were detected. According to the EDS line graph in Figure 6(c), the concentration of Fe in the layer immediately adjacent to the steel surface is higher than for Ca, whereas the layer on the outer surface has the opposite relationship. Recall that the XRD data shows two distinct phases:  $\text{Fe}_x\text{Ca}_y\text{CO}_3$  and  $\text{CaCO}_3$ . Taken in conjunction with the cross-sectional analysis, this would imply that a bilayer structure had formed with  $\text{CaCO}_3$  scale growing from the surface of the  $\text{Fe}_x\text{Ca}_y\text{CO}_3$  corrosion

product. Figure 6(d), the cross-sectional analysis of the experiment with 10,000 ppm  $\text{Ca}^{2+}$ , does not show an obvious bilayer structure at the steel surface. There is, however, a significant Ca/Fe concentration gradient, consistent with the XRD data. There seems to be an increased “roughening” of the steel surface as the  $\text{Ca}^{2+}$  concentration increases; however, this is better seen in the images below taken after the surface layer was removed.

Figure 7 shows SEM images of the surface after specimens were treated with Clarke's solution, which completely removed the surface layer. General roughening of the surface is confirmed, as the  $\text{Ca}^{2+}$  concentration is increased. At the highest  $\text{Ca}^{2+}$  concentration of 10,000 ppm there appears to be some initiation of

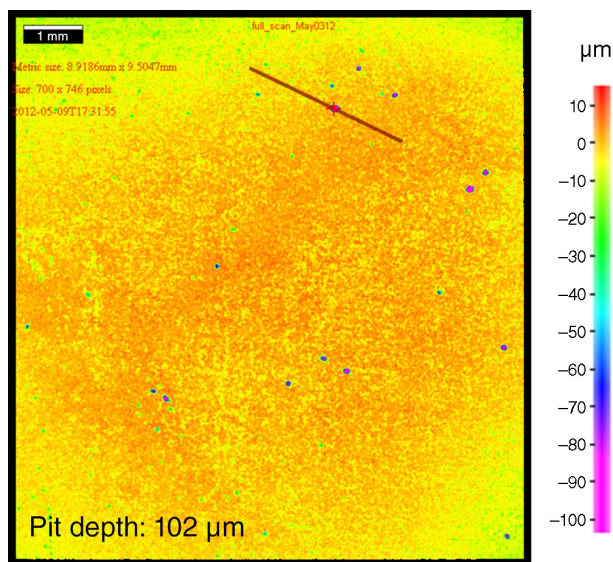


**FIGURE 8.** IFM of sample (UNS G10180) after removal of corrosion product for the experiment conducted at 80°C and  $p\text{CO}_2$  0.05 MPa with 10 ppm  $\text{Fe}^{2+}$  + 10,000 ppm  $\text{Ca}^{2+}$ .

pitting; however, this is difficult to judge because of the relatively short duration of the experiments. The calculated maximum penetration rate, according to deepest pit found by the IFM analysis, is 6.0 mm/y, as shown in Figure 8. This is significantly higher than the average uniform corrosion rate detected by LPR, Figure 1(a).

## CONCLUSIONS

❖  $\text{CO}_2$  storage into saline aquifers in the long term can lead to the decrease in pressure of  $\text{CO}_2$ , which leads to the formation of  $\text{CO}_2$  gas. As such,  $\text{CO}_2$  gas interacts with water and  $\text{Ca}^{2+}$  in the brine. The preliminary study of the calcium effect on  $\text{CO}_2$  corrosion at low pressure was done, and this study showed that mild steel exposed to electrolytes that contain  $\text{Ca}^{2+}$  at 0.5 bar  $\text{CO}_2$  and 80°C, with a pH of 6.5, leads to the formation of  $\text{Fe}_x\text{Ca}_y\text{CO}_3$  ( $x + y = 1$ ) on the surface. The formation of this mixed metal carbonate at high  $\text{Ca}^{2+}$  concentrations changes the corrosion behavior of the mild steel.  $\text{Ca}^{2+}$  affected the corrosion behavior by changing the water chemistry, particularly as the formation of non-protective  $\text{CaCO}_3$  interfered with the formation of protective  $\text{FeCO}_3$ . At low concentrations of  $\text{Ca}^{2+}$ , although it incorporates into the  $\text{FeCO}_3$  structure, the calcium does not significantly change the properties of  $\text{FeCO}_3$ . However, at higher  $\text{Ca}^{2+}$  concentrations, the characteristics and behavior of the corrosion product layer changed significantly. At 10,000 ppm  $\text{Ca}^{2+}$ , XRD data showed the formation of  $\text{CaCO}_3$  with the incorporation of  $\text{Fe}^{2+}$  into the structure, concomitant with non-uniform corrosion attack.

## ACKNOWLEDGMENTS

The authors would like to thank B. Brown for his support of this study. The financial support of the Department of Chemical and Biomolecular Engineering is appreciated.

## REFERENCES

1. J. Gale, J. Davison, *Energy* 29 (2004), p. 1319-1328.
2. A.M. Nor, M.F. Suhor, M.F. Mohamed, M. Singer, S. Nešić, "Corrosion of Carbon Steel in High  $\text{CO}_2$  Environment: Flow Effect," CORROSION/2011, paper no. 11242 (Houston, TX: NACE International, 2011).
3. Y.S. Choi, S. Nešić, "Effect of Water Content on the Corrosion Behavior of Carbon Steel in Supercritical  $\text{CO}_2$  Phase with Impurities," CORROSION/2011, paper no. 11377 (Houston, TX: NACE, 2011).
4. A. Dugstad, "Mechanism of Protective Film Formation During  $\text{CO}_2$  Corrosion of Carbon Steel," CORROSION/98, paper no. 31 (Houston, TX: NACE, 1998).
5. R. Nyborg, "Initiation and Growth of Mesa Corrosion Attack During  $\text{CO}_2$  Corrosion of Carbon Steel," CORROSION/98, paper no. 48 (Houston, TX: NACE, 1998).
6. S. Nešić, M. Nordsveen, R. Nyborg, A. Stangeland, *Corros. Sci.* 59 (2003): p. 489-497.
7. J. Han, B. Brown, S. Nešić, *Corrosion* 66 (2010): p. 1-12.
8. J.K. Heuer, J.F. Stubbins, *Corros. Sci.* 41 (1999): p. 1231-1243.
9. S. Nešić, *Corros. Sci.* 49 (2007): p. 4308-4338.
10. M.B. Kermani, A. Morshed, *Corrosion* 59 (2003): p. 659-683.
11. S. Nešić, L. Lunde, *Corros. Sci.* 50 (1994): p. 717-727.
12. R. De Marco, Z.T. Jiang, B. Pejčić, E. Poinen, *J. Electrochem. Soc.* 152 (2005): p. B389-B392.
13. G.F. Lin, M.S. Zheng, Z.-Q. Bai, Y.R. Feng, *J. Iron. Steel Res. Int.* 13 (2006): p. 47-52.
14. G. Schmitt, M. Hörstemeier, "Fundamental Aspects of  $\text{CO}_2$  Metal Loss Corrosion—Part II: Influence of Different Parameters on  $\text{CO}_2$  Corrosion Mechanisms," CORROSION/2006, paper no. 06112 (Houston, TX: NACE, 2006).
15. F. Yu, K.W. Gao, Y.J. Su, J.X. Li, L.J. Qiao, W.Y. Chu, M.X. Lu, *Mater. Lett.* 59 (2005): p. 1709-1713.
16. Z.D. Cui, S.L. Wu, S.L. Zhu, X.J. Yang, *Appl. Surf. Sci.* 252 (2006): p. 2368-2374.
17. B. Ingham, M. Ko, N. Laycock, J. Burnell, P. Kappen, J.A. Kimpton, D.E. Williams, *Corros. Sci.* 56 (2012): p. 96-104.
18. J.E. Wajon, G.-E. Ho, P.J. Murphy, *Water Res.* 19 (1985): p. 831-837.
19. T. Li, Y. Yang, K. Gao, M. Lu, *J. Univ. Sci. Technol. Beijing, Min. Metall. Mater.* 15 (2008): p. 702-706.
20. C.A. Palacios, J.R. Shadley, *Corrosion* 47 (1991): p. 122-127.
21. M. Gao, X. Pang, K. Gao, *Corros. Sci.* 53 (2011): p. 557-568.
22. B. Zerai, B.Z. Saylor, G. Matisoff, *Appl. Geochem.* 21 (2006): p. 223-240.
23. G.X. Zhao, J.P. Li, S.M. Hao, X.H. Lu, H.L. Li, *J. Iron Steel Res. Int.* 12 (2005): p. 35-53.
24. G.X. Zhao, X.H. Lu, J.M. Xiang, Y. Han, *J. Iron. Steel Res. Int.* 16 (2009): p. 89-94.
25. C. Ding, K.W. Gao, C.F. Chen, *Int. J. Miner. Metall. Mater.* 16 (2009): p. 661-666.
26. X. Jiang, Y.G. Zheng, D.R. Qu, W. Ke, *Corros. Sci.* 48 (2006): p. 3091-3108.
27. C.Q. Ren, X. Wang, L. Liu, H.E. Yang, N. Xian, *Mater. Corros.* 63 (2012): p. 168-172.
28. S.D. Zhu, J.F. Wei, Z.Q. Bai, G.S. Zhou, J. Miao, R. Cai, *Eng. Fail. Anal.* 18 (2011): p. 950-962.
29. K. Gao, F. Yu, X. Pang, G. Zhang, L. Qiao, W. Chu, M. Lu, *Corros. Sci.* 50 (2008): p. 2796-2803.
30. ASTM G1-03(2011), "Standard Practice for Preparing, Cleaning, and Evaluating Corrosion Test Specimens" (West Conshohocken, PA: ASTM International, 2011).
31. M. Nordsveen, S. Nešić, R. Nyborg, A. Stangeland, *Corros. Sci.* 59 (2003): p. 443-456.
32. B.F.M. Pots, S.D. Kapusta, "Prediction of Corrosion Rates of the Main Corrosion Mechanisms in Upstream Applications," CORROSION/2005, paper no. 05550 (Houston, TX: NACE, 2005).
33. S. Nešić, "Carbon Dioxide Corrosion of Mild Steel," ed. R.W. Revie, in *Uhlig's Corrosion Handbook*, 3rd ed. (Hoboken, NJ: Wiley, 2011), p.229-245
34. W. Sun, S. Nešić, *Corrosion* 64 (2008): p. 334-346
35. L. Plummer, E. Busenberg, *Geochim. Cosmochim. Acta* 46 (1982): p. 1011-1040.